Supporting information (SI) for the paper:

Supramolecular Functionalization and Concomitant Enhancement in Properties of Au_{25} Clusters

Ammu Mathew, Ganapati Natarajan, Lauri Lehtovaara, Hannu Häkkinen, Ravva Mahesh Kumar[‡], Venkatesan Subramanian[‡], Abdul Jaleel[#] and Thalappil Pradeep[*]

DST Unit of Nanoscience (DST UNS) and Thematic Unit of Excellence (TUE), Department of Chemistry, Indian Institute of Technology Madras, Chennai 600036, India.

Departments of Chemistry and Physics, Nanoscience Center, University of Jyväskylä, Finland.

[‡]*Chemical Laboratory, CSIR-Central Leather Research Institute, Adyar, Chennai 600020, India.*

[#]*Proteomics Core Facility, Rajiv Gandhi Centre for Biotechnology, Thiruvananthapuram 695014, India*

[*]E-mail: pradeep@iitm.ac.in

Table of contents

Supporting information 1

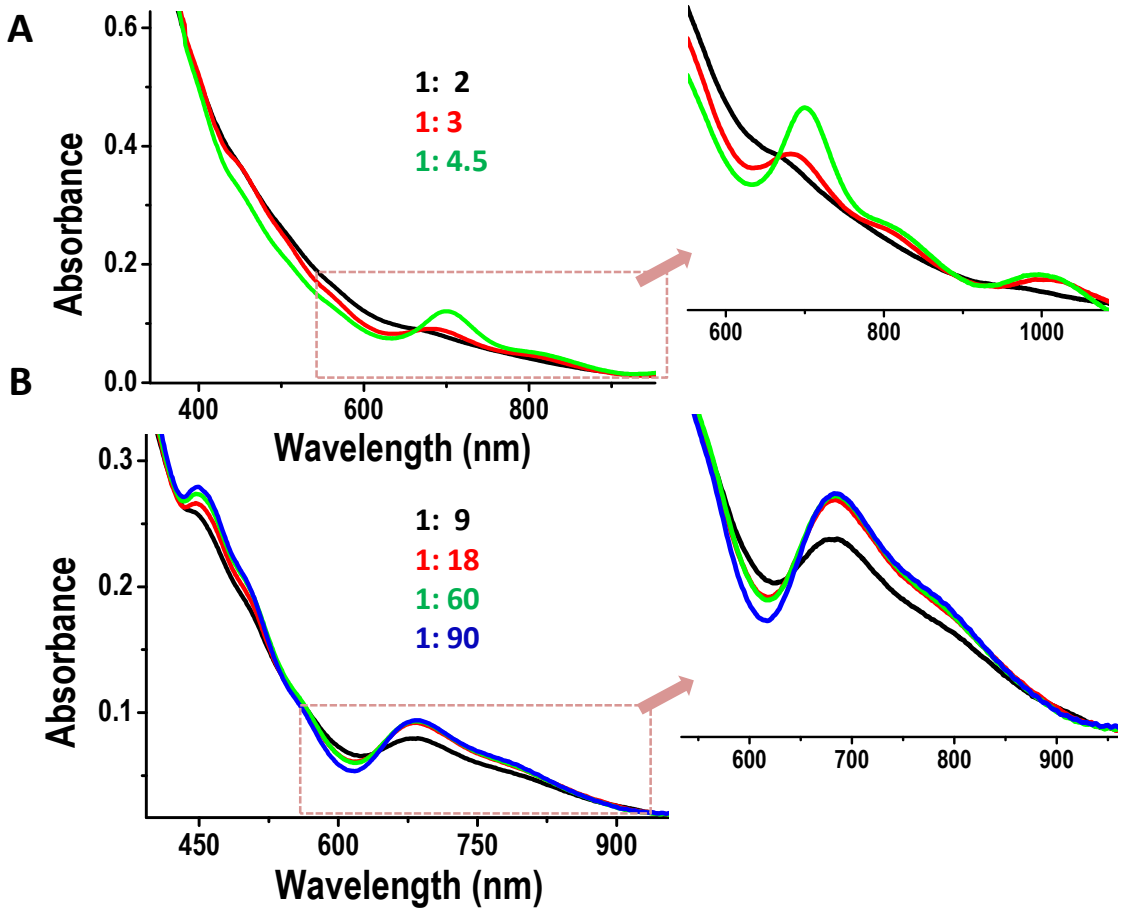

Figure S1. Effect of UV-vis optical absorption spectra for various Au:BBSH ratios used for cluster synthesis. An optimum Au:S ratio of 1:6 was employed for typical synthesis of $Au_{25}SBB_{18}$ (see Figure 1 in paper). While lower thiol ratios (A) showed significant changes in the absorption profile indicating that clusters of higher core sizes are getting formed, even a ten fold increase in thiol (B) compared to the optimised synthesis did not seem to yield still smaller clusters.

Supporting information 2

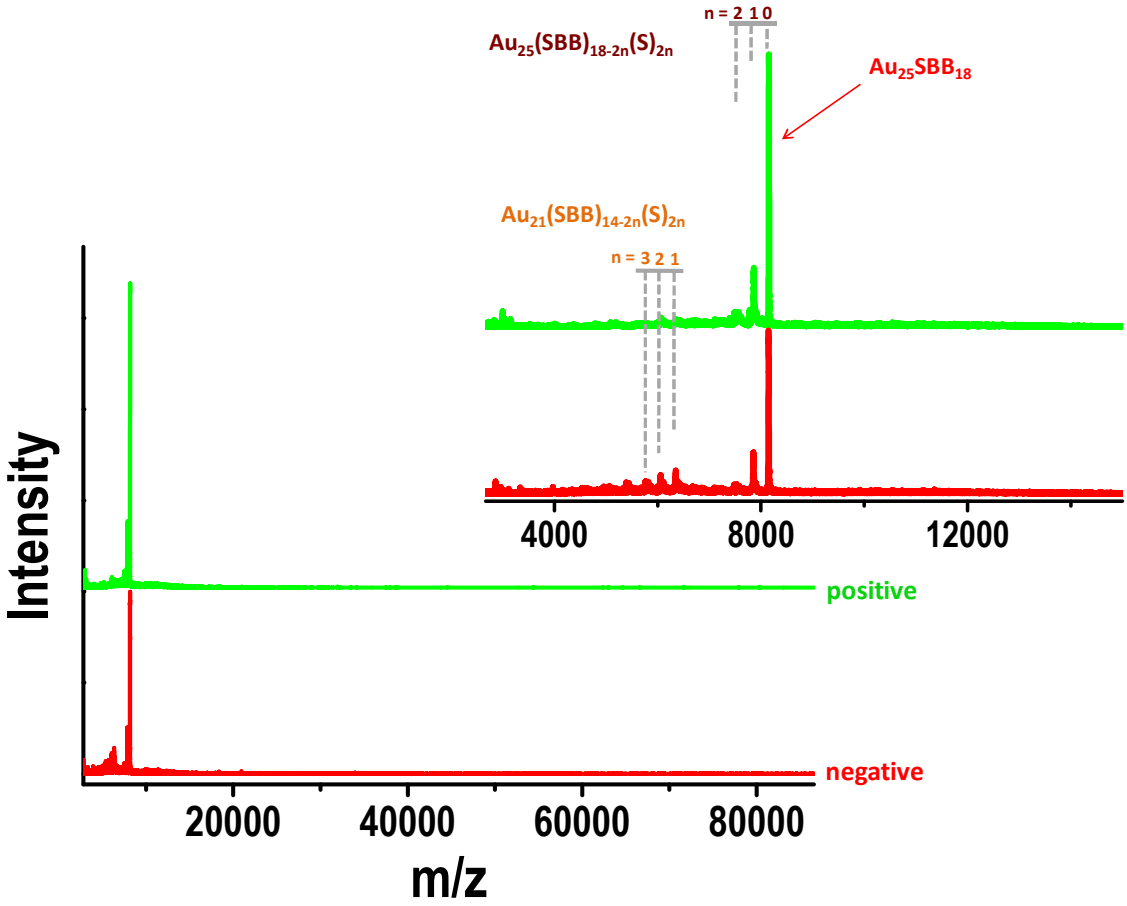

Figure S2. Full range MALDI (L) mass spectra of $Au_{25}SBB_{18}$ cluster in both positive and negative ion modes. Fragmentation due to the C-S cleavage of SBB ligand on the cluster surface can be observed apart from the molecular ion peak (these features are expanded in the inset). Loss of $[Au_4L_4]$ fragment from the parent cluster is a typical phenomenon in Au_{25} clusters. Here, we observed similar fragments corresponding to $[Au_4SBB_4BB_{2n}]$ loss, where n = 1, 2, 3 in the negative ion mode from parent $Au_{25}SBB_{18}$. The additional BB losses observed in the negative mode (red trace in inset) could be due to the facile C-S cleavage as in the case of the molecular ion peak at 8151 Da. DCTB was used as the matrix and threshold laser intensities were employed for all the measurements.

Supporting information 3

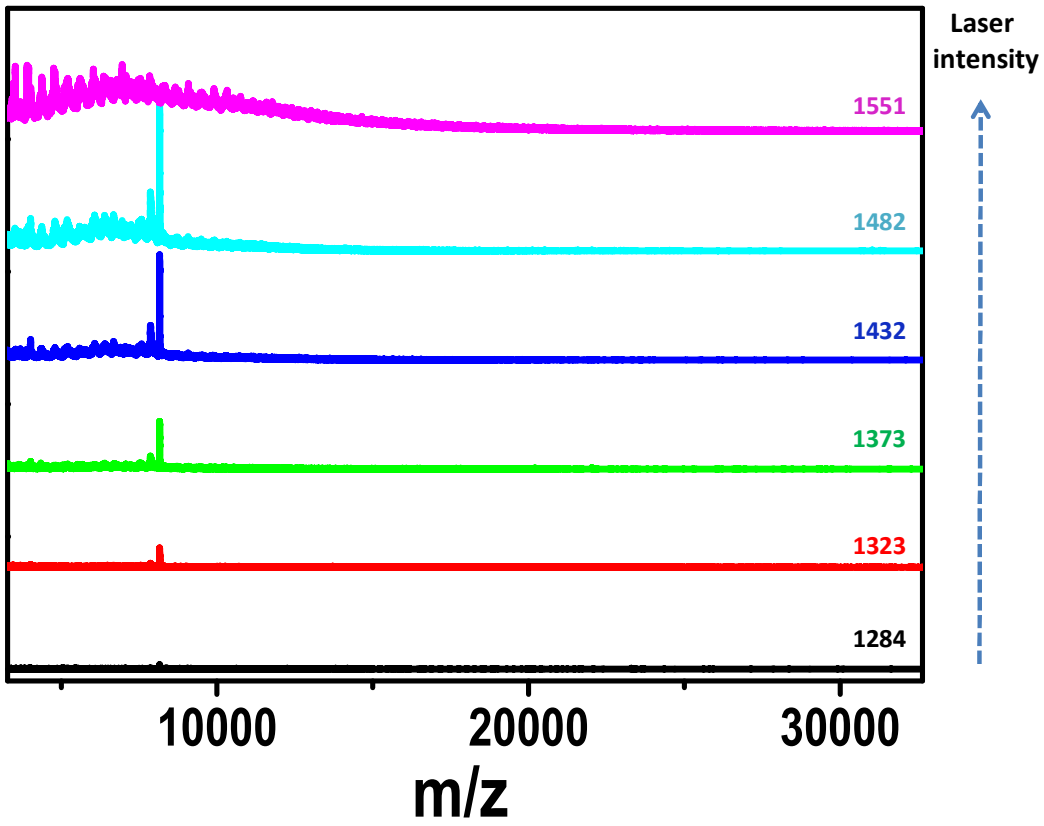

Figure S3. MALDI (L) mass spectra of the purified $Au_{25}SBB_{18}$ cluster at different laser intensities in the positive mode. Control over the laser intensity is vital to observe the molecular ion peak of the cluster without fragmentation. Laser intensity (shown at the right extreme) is as given by the instrument and has not been calibrated to a standard unit.

Supporting information 4

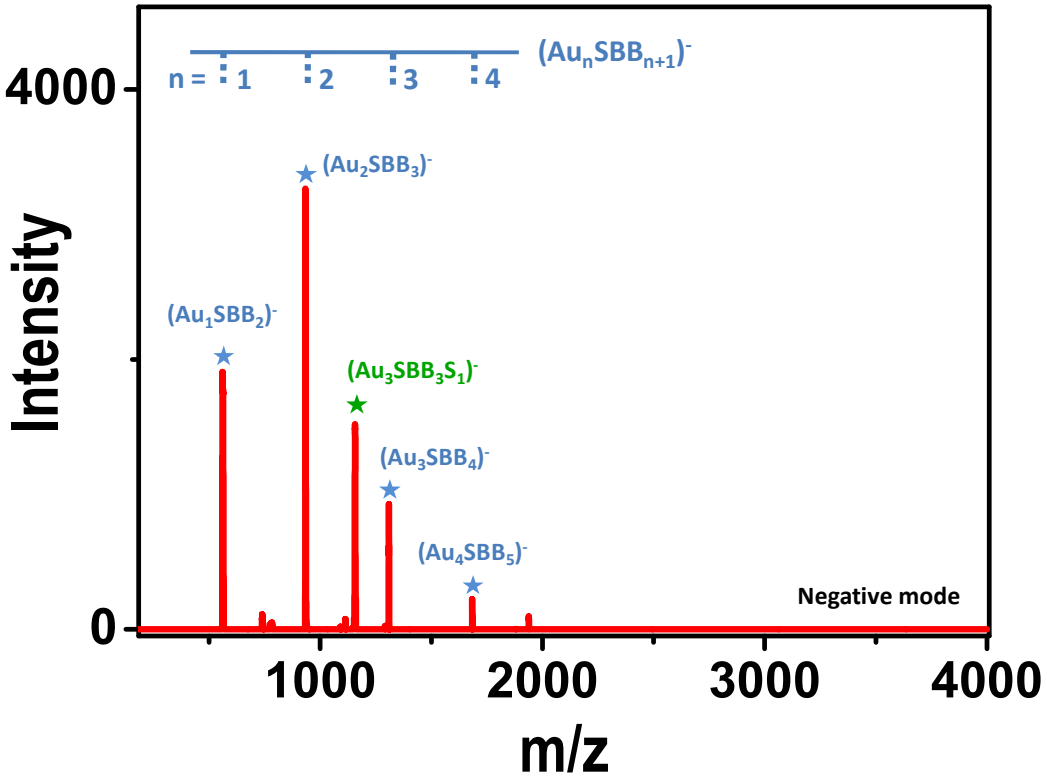

Figure S4. ESI MS of $Au_{25}SBB_{18}$ in negative ion mode showing fragments from the cluster in the low mass region.

Supporting information 5

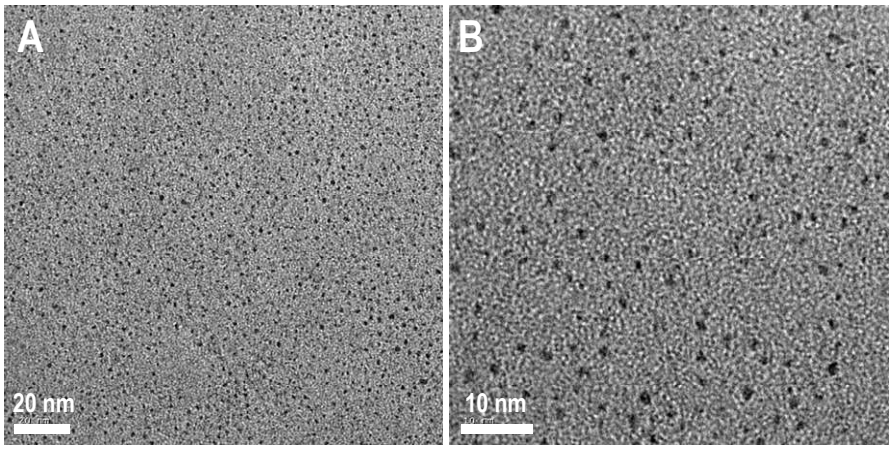

Figure S5. TEM images of $Au_{25}SBB_{18}$. Two magnifications are shown. Unlike in typical thiolated clusters, these samples are resistant to electron beam induced aggregation.

Supporting information 6

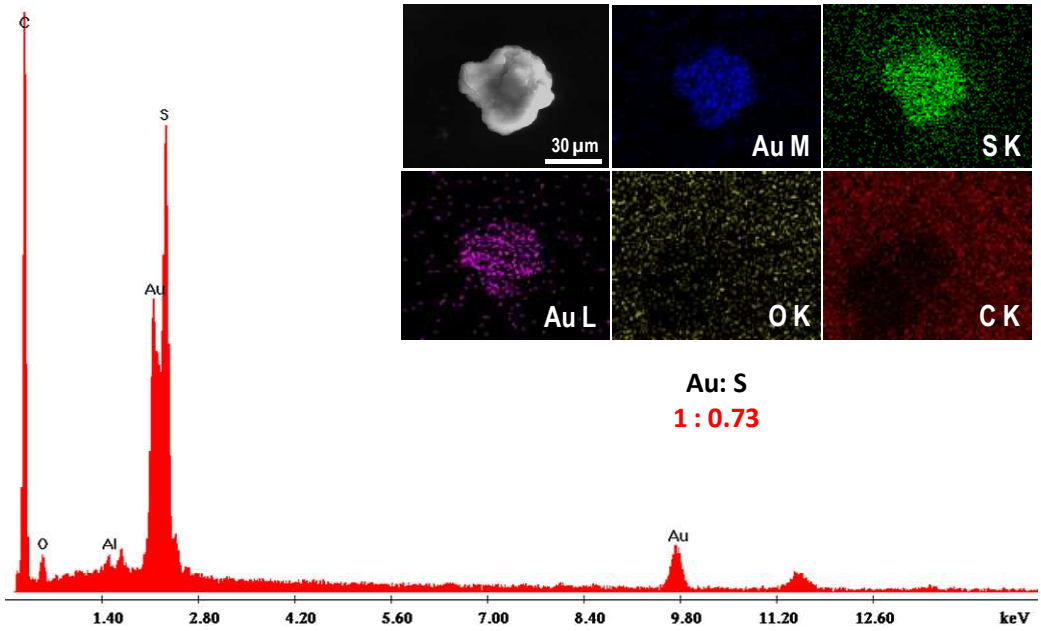

Figure S6. SEM and EDAX characterization of $Au_{25}SBB_{18}$ cluster. Carbon and aluminium are from the substrate used for the measurement. Contrast of carbon is low due to the use of carbon tape as the substrate. The scale is same for all images.

Supporting information 7

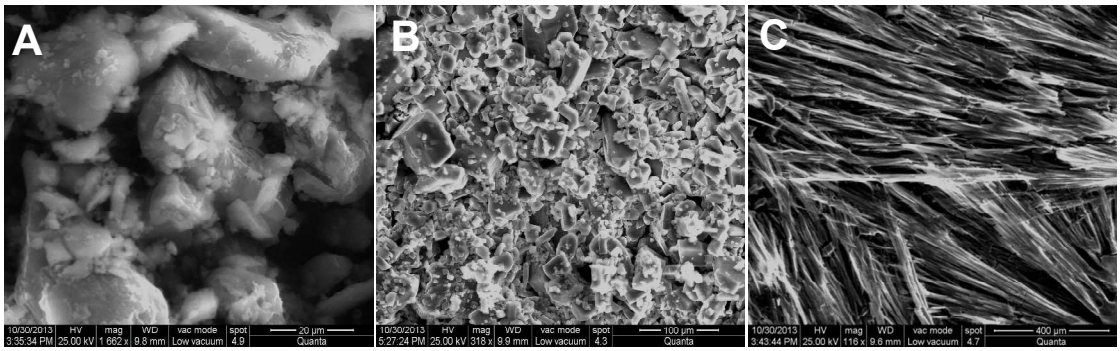

Figure S7. SEM images of (A) native β-CD powder, (B) drop cast β-CD solution in water and (C) drop cast β-CD solution in THF:water (30:1) mixture, after sonication. The formation of needle-like superstructures by self assembly occurred only in the case of reaction in THF:water (30:1) solvent mixture. Presence of minimal amount of water molecules can enhance the possibility of intermolecular hydrogen bonding between the hydroxyl group present on the outer rim of CD molecules. Control experiments in water (B), did not result in formation of superstructures. Thus the dispersion of β-CD molecules by sonication in THF and their subsequent self assembly by re-formation of the strong hydrogen bonding between the CDs with the aid of THF results in these superstructures.

Supporting information 8

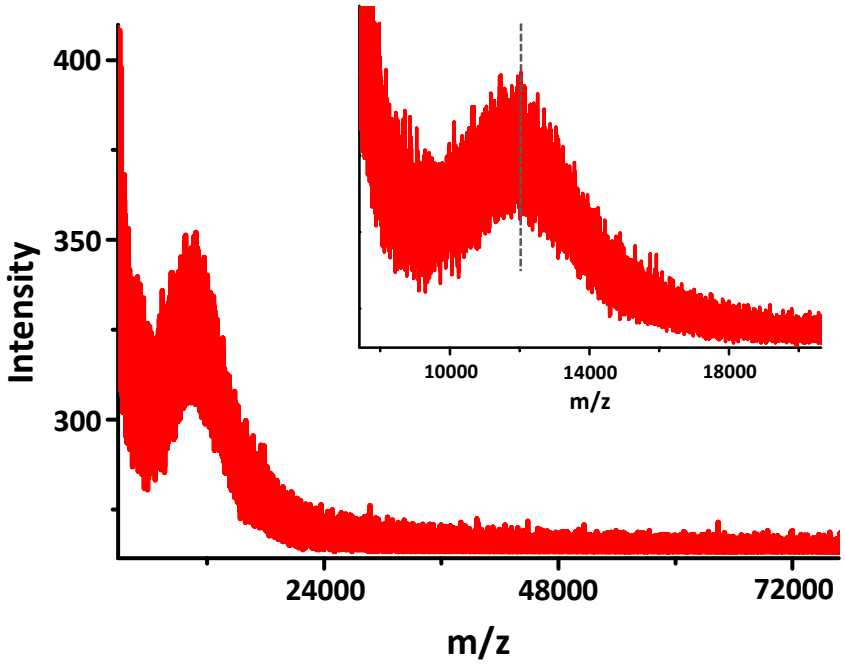

Figure S8. LDI mass spectrum of the aqueous layer, post synthesis of the CD-functionalised $Au_{25}SBB_{18}$ clusters. Addition of excess water to the microtubular arrangement of CD and cluster leads to the formation of $Au_{25}SBB_{18}\cap CD_n$ (where n=1-4). Though we found better mass spectral intensities for the adducts from the organic layer (see Figure 2 in main text), probably due to the existence of more number of hydrophobic SBB groups on the cluster surface (18-n, where n<4), analysis of the aqueous layer showed a broad peak at higher mass range too albeit with reduced intensity. Inset shows an expanded view. Peak maximum corresponding to $Au_{25}SBB_{18}\cap CD_4$ is marked with a line.

Supporting information 9

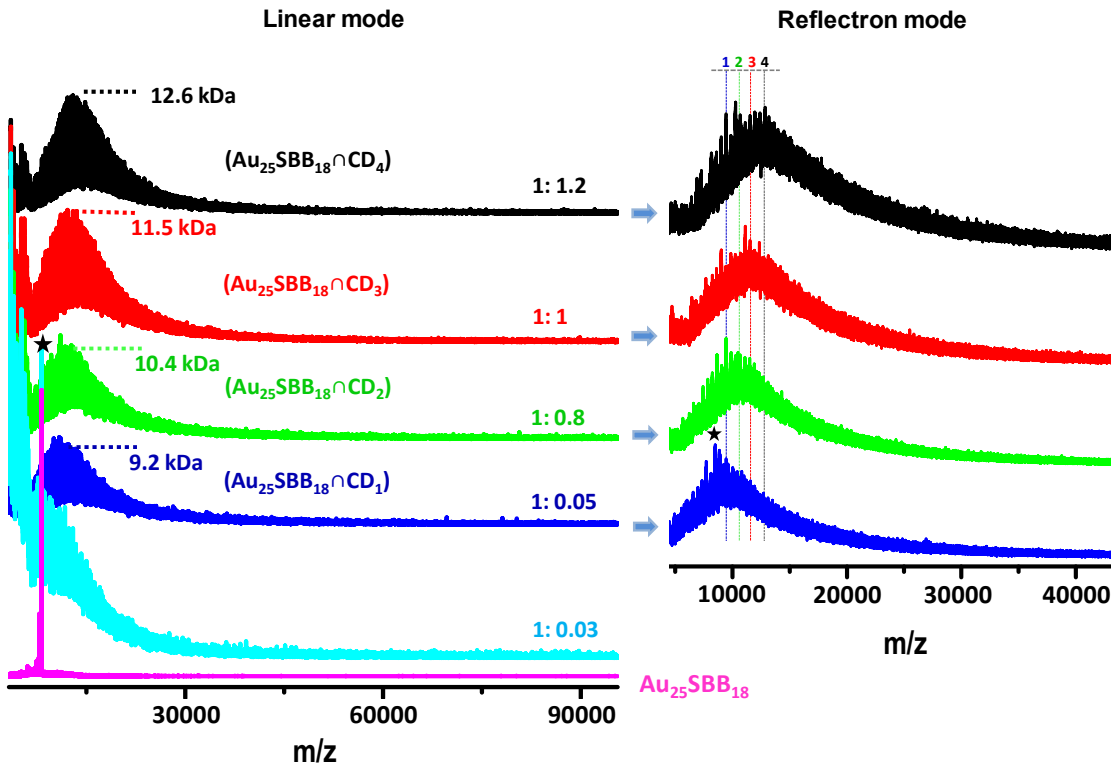

Figure S9. Positive mode MALDI (L) and MALDI (R) mass spectra of $Au_{25}SBB_{18}$ with increasing SBB:CD ratios in solution. The peak maxima shift with increasing BBS:CD ratio. This gradual increase is marked. Peak corresponding to parent $Au_{25}SBB_{18}$ is marked using a *. These peak positions are the same in both the data sets, but in the reflectron mode the peaks are better resolved as the resolution is improved. These peaks resolve even better in the MALDI TOF TOF mode (see S10).

Supporting information 10

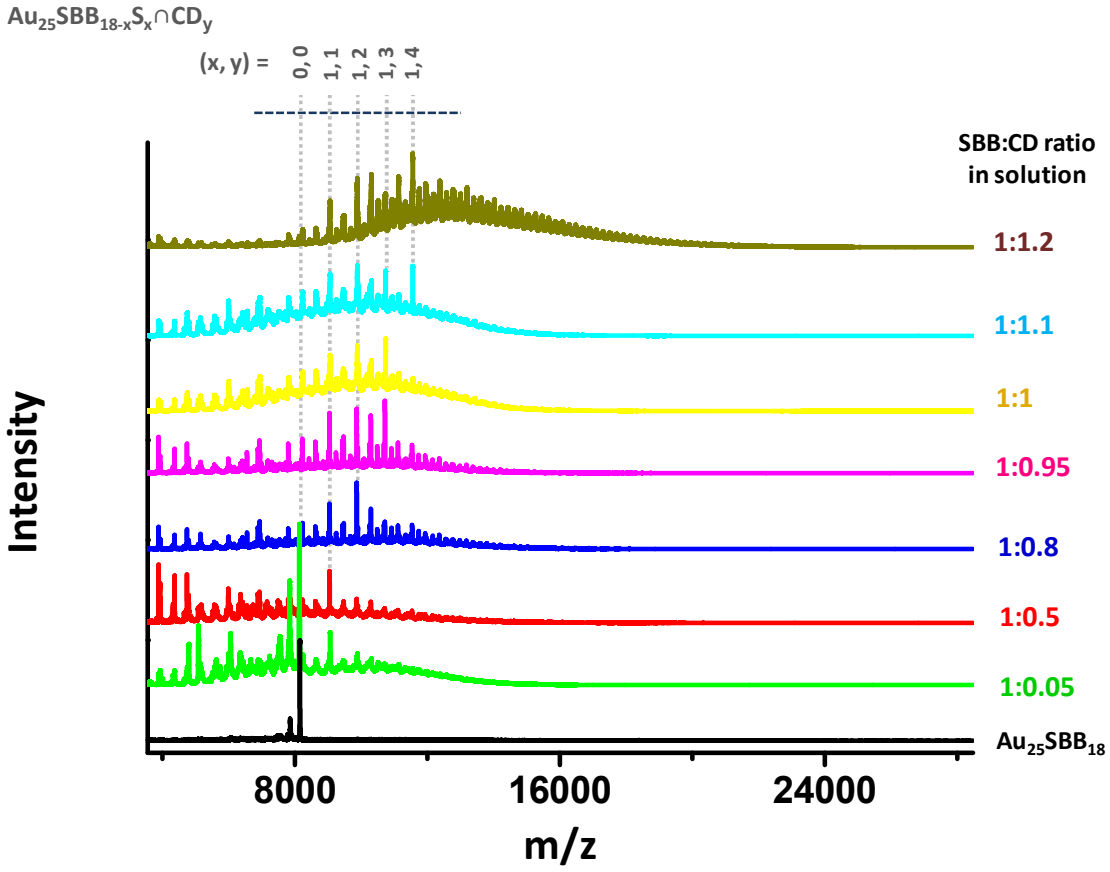

Figure S10. MALDI TOF TOF mass spectra of $Au_{25}SBB_{18}$ with increasing SBB:CD ratios (green to brown) in solution. The peaks are better resolved than in S9.

Supporting information 11

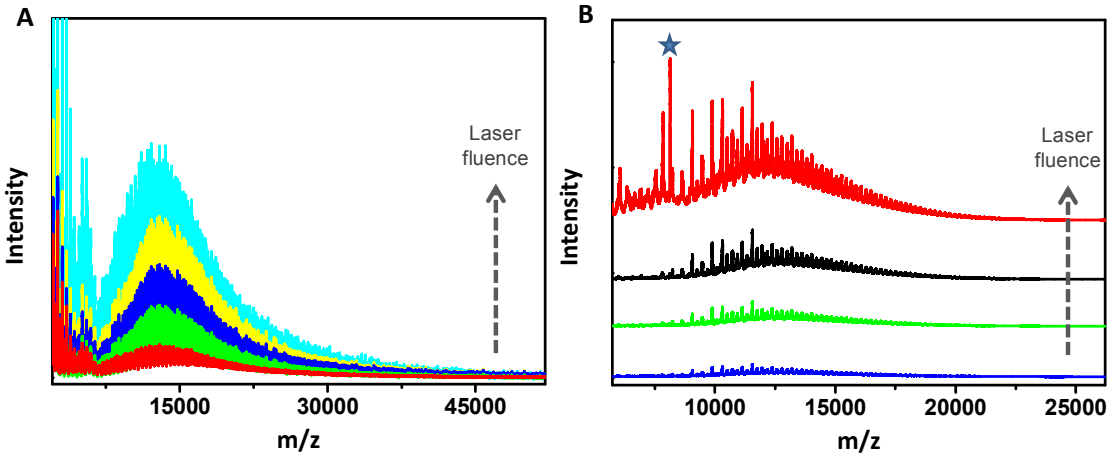

Figure S11. MALDI (L) mass spectra (A) and MALDI TOF TOF mass spectra (B) of $Au_{25}SBB_{18}\cap CD_4$ at different laser intensities in the positive mode. Note that though the background of the spectra increases with more laser fluence, the peak maxima and relative individual peak intensities remain the same except for red trace in (B) wherein peak due to $Au_{25}SBB_{13}S_5$ (marked with a *) gain intensity at higher laser fluence due to cleavage of C-S bond and loss of CDs. There are threshold laser powers above which fragmentations occur.

Supporting information 12

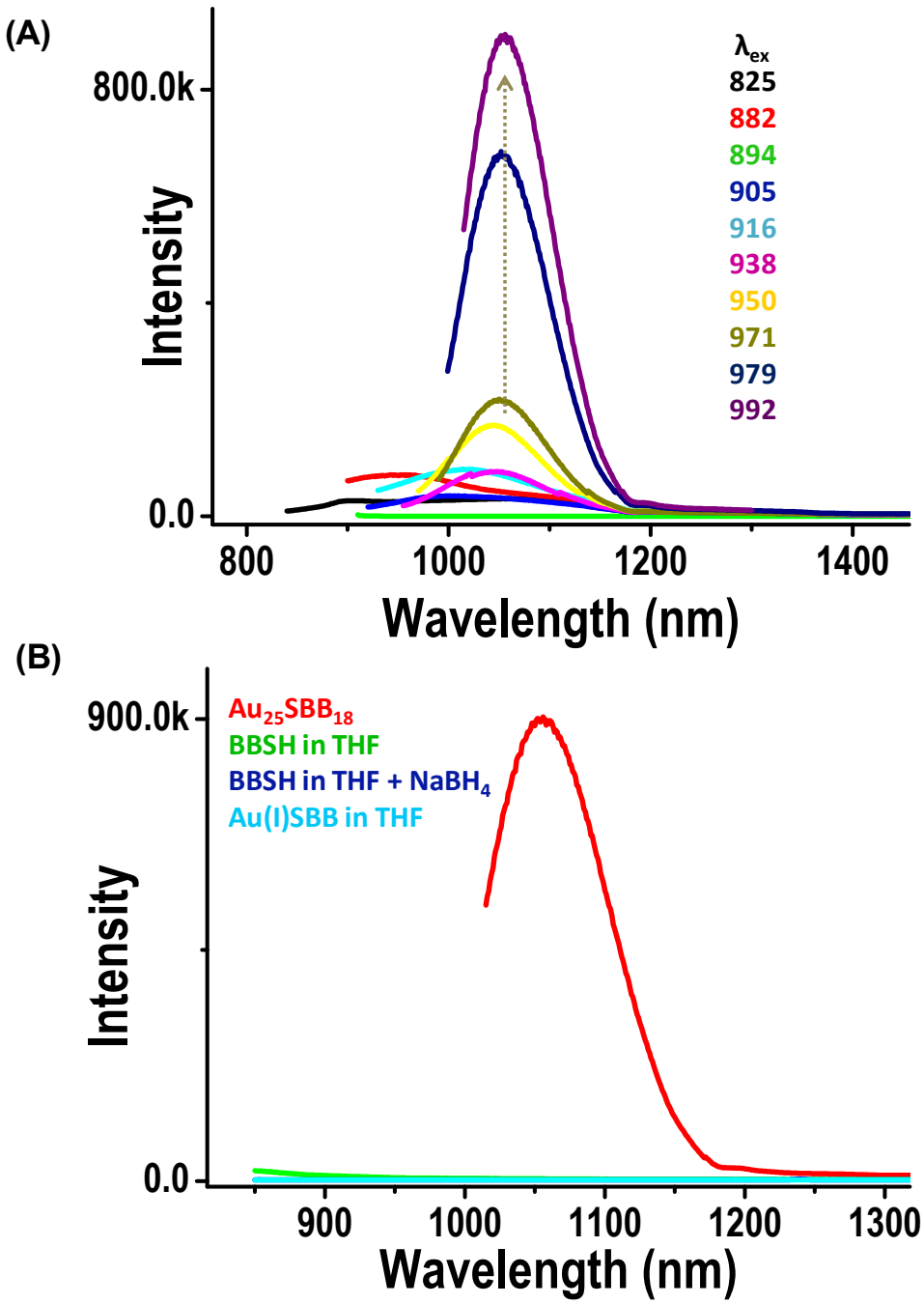

Figure S12. NIR luminescence observed from the bare $Au_{25}SBB_{18}$ cluster at (A) various excitation wavelengths and (B) comparison with the spectra (λ_{ex} 992 nm) of various starting materials.

Supporting Information 13

Structural optimization of $Au_{25}SBB_{18}$

The cluster was rotated so that the *x*-axis lay along the axis of the cluster passing through its center and the bridging sulfur atoms which were spaced the furthest distance apart.

Cluster boundary conditions were used and the size of the simulation box was chosen to be 34 Å, leaving about 9 Å of buffer space around the molecule. A negative charge was added to the molecule.

$Au_{25}SBB_{18}\cap CD_4$

Ligand structure of $Au_{25}SBB_{18}$ and CD attachment

The precise arrangement around any given ligand will affect whether that ligand may be a likely one for CD complexation. It was observed that bridging ligands were generally surrounded by ligands which were quite close to it, while the ligands neighboring a non-bridging ligand were spread further apart. The number of nearest-neighbor ligands to a CD centered on a chosen ligand was four.

The model of $Au_{25}SBB_{18}\cap CD_4$ was constructed by making attachments of CDs to the DFT optimized structure of $Au_{25}SBB_{18}$ using molecular builder software. The narrow side of the CD was attached first as this would reduce steric hindrance and this configuration had a lower binding energy as an isolated complex. The choice of ligands also affects the depth of penetration of the CD onto the ligand, which is lesser in the case of the bridging ligands due to greater steric hindrance from the neighbouring ligands. For non-bridging ligands both the aromatic BBS protons and *t*-butyl group protons would be close to the inner CD protons, which also agrees with the NMR data. For bridging ligands the inner H^3 and H^5 protons of the CD would be closer to the *t*-butyl groups.

The non-bridging ligand denoted by *(y,-z)*, in the notation described in the main paper, was easily accessible due to the widely separated positions of the surrounding ligands and hence was chosen for making the first attachment of the CD. The attachment was made in a stepwise fashion starting by including the *t*-butyl group and then by bringing the narrow end of the CD further over the ligand and then reoptimizing using a UFF force field until its position was in agreement with the NMR data. We also rejected position changes which increased the total energy. During the optimization, the core and staple atoms, *i.e.* the Au and S atoms, were kept fixed in their positions from DFT, while the other atoms were allowed to move. This process was repeated three more times by making CD attachments to the *(-z, -x), (x,-y) and (z,-x)* non-bridging ligands which were easily accessible. The energy of the final structure in the UFF force field was 60,323 kcal/mol.
From our calculations on BBSH∩CD, it is energetically favourable for the included ligand to be at an angle with respect to the CD. Tilting the CD to the angles found in the optimized geometries of BBSH∩CD was found difficult due to the presence of the neighboring ligands. The relative angle of the CD and included ligand varies due to the differing orientations of the included ligand and its neighbors. We remark here that further force-field calculations and molecular dynamics simulations would be necessary to determine more precise attachment

geometries as several different configurations which differ in depth and angle of attachment are consistent with the NMR data.

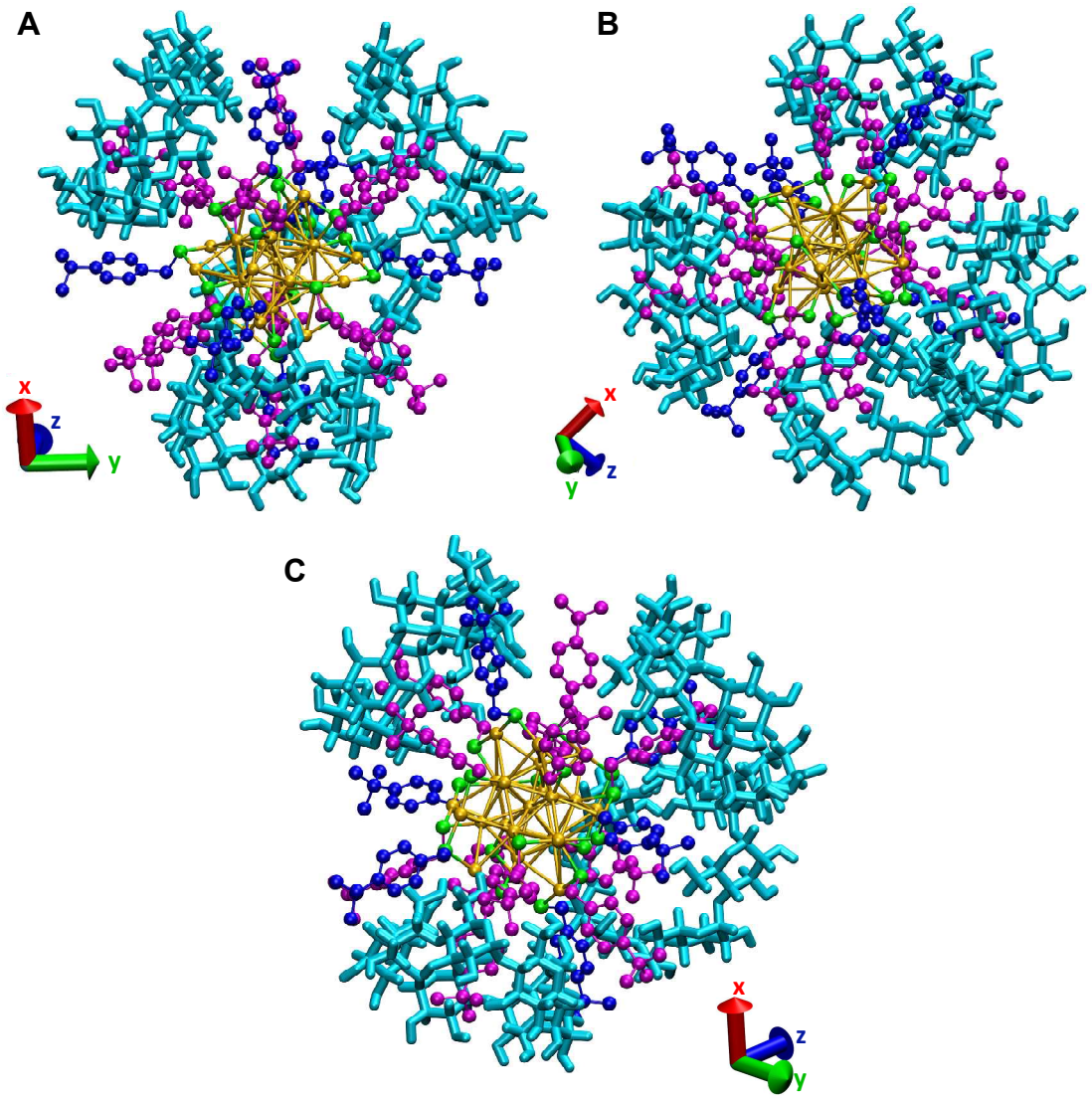

Figure S13. Different views of the $Au_{25}SBB_{18}\cap CD_4$ model. Hydrogen atoms are not shown on the SBB ligands for clarity. Sulfur and gold atoms are shown in green and gold, respectively, while the carbon atoms of the bridging and non-bridging ligands are shown in blue and magenta, respectively. The four attached CDs are shown in cyan in the stick molecular representation. The cartesian *x*, *y*, and *z* axes are shown by the red, green and blue arrows, respectively.

DFT calculations on BBSH∩CD

In this section we give full details of the DFT calculations performed on the BBSH∩CD inclusion complexes and discuss some of the theoretical results presented in the paper in

more detail. All calculations were performed with the Gaussian 09 code.[1] The experimental structure of β-cyclodextrin ($C_{70}H_{42}O_{35}$) was obtained from the Hic-Up Database and was based on the Protein Data Bank file pdb1z0n.ent.[2] As the downloaded structure was without hydrogen atoms these were added to this structure and the hydrogen positions were optimized at B3LYP/6-31G* keeping all the other atoms fixed in the same positions as experiment. The geometry of BBSH molecule ($C_{11}H_{15}SH$) was obtained from the web database ChemSpider.[3] A geometry optimization at the B3LYP/6-311+G** level was carried out. The optimization resulted in small changes in the geometry, as the plane of the benzene ring rotated to be perpendicular to the plane containing the C_1-C_2 bond (carbons are numbered starting from the sulfur end).

The above geometries of CD and BBSH were then used for creating the initial configurations of two BBSH∩CD adducts. The BBSH molecule was inserted into the CD cavity with the *t*-butyl group going in first. The alignment of the BBSH molecule was such that its C_1-C_2 axis was along the axis of the CD passing through the CD centre and perpendicular to the planes of its openings. Two such initial configurations were constructed by insertion into the wide and narrow ends of the CD. The geometry optimizations were carried out using the meta-GGA hybrid functional m052-X, which describes more accurately the non-covalent interactions found in the adducts, in conjunction with 6-31G* and 6-31+G** basis sets. During the optimization, the CD atoms were kept fixed and only the BBSH atoms were allowed to move. This was done not only to speed up the computations but also because β-CD adopts what is known as the anhydrous configuration after a full DFT geometry optimization,[4] which is different from its structure in a solvent.

The optimized geometries of the adducts are shown in Figure 4D (narrow end entry) and 4E (wide end entry), indicating the stability of these adducts due to non-covalent interactions. We did not find a significant change in the geometries with increase in the size of the basis set, and we have presented results using 6-31G* in Figures 4D and 4E. The BBSH molecule adopted a slanted configuration with its C_1-C_2 axis parallel to the side of the CD in both the narrow and wide entry cases. Binding energies of the narrow and wide entry configurations were performed using the Boys counterpoise correction method[5] with the m052-X/6-31+G** level of theory. The binding energy is about 2 kcal/mol less for the narrow case. We might attribute this to stronger π-bonding between the BBSH aromatic ring and the inner CD protons in the narrow case because of the shorter inter-proton distance caused by the narrowing of the profile of the CD.

A careful note of the relative positions of BBSH and CD protons was made in order that agreement with NMR experimental data might be evaluated. Referring to Figure 4D and 4E we see the following. In the narrow case, the H^b group protons are located around the level of the O-H^1 protons, the lower aromatic H^c protons (closest to the sulfur end) are around the level of the H^2 protons of CD, the upper aromatic H^d protons are situated around the level of the H^3 CD protons, while the *t*-butyl group H^e protons are situated between the level of the H^5 and H^6 CD protons. In the wide case, the H^b protons are slightly below the H^6 protons and not inside the CD, the lower aromatic H^c protons are at the H^5 proton level, the upper aromatic H^d protons are the at H^3 proton level, while the *t*-butyl group H^e protons are between the H^5, H^6 and H^7 protons.

NMR data suggests an interaction between both the aromatic and *t*-butyl group protons of BBSH with the H^3 and H^5 inner CD protons, which is also in good general agreement with both the structures. However it is not possible to identify the specific NMR fingerprints of

each of the structures from the experimental data which suggests the possibility of NMR calculations at DFT level. The arrangement of the included ligand and the CD were found to be different for inclusion complexes formed with ligands attached to the cluster rather than isolated ligands. Firstly, the presence of a gold core and -Au-S-Au-S-Au- staples attached to the sulfur of the SBB ligand decreases the penetration depth of the CD. Secondly, the steric hindrance caused by the presence of about four or five ligands around the CD decreases both the CD penetration depth and the angle between the CD and the ligand.

Supporting information 14

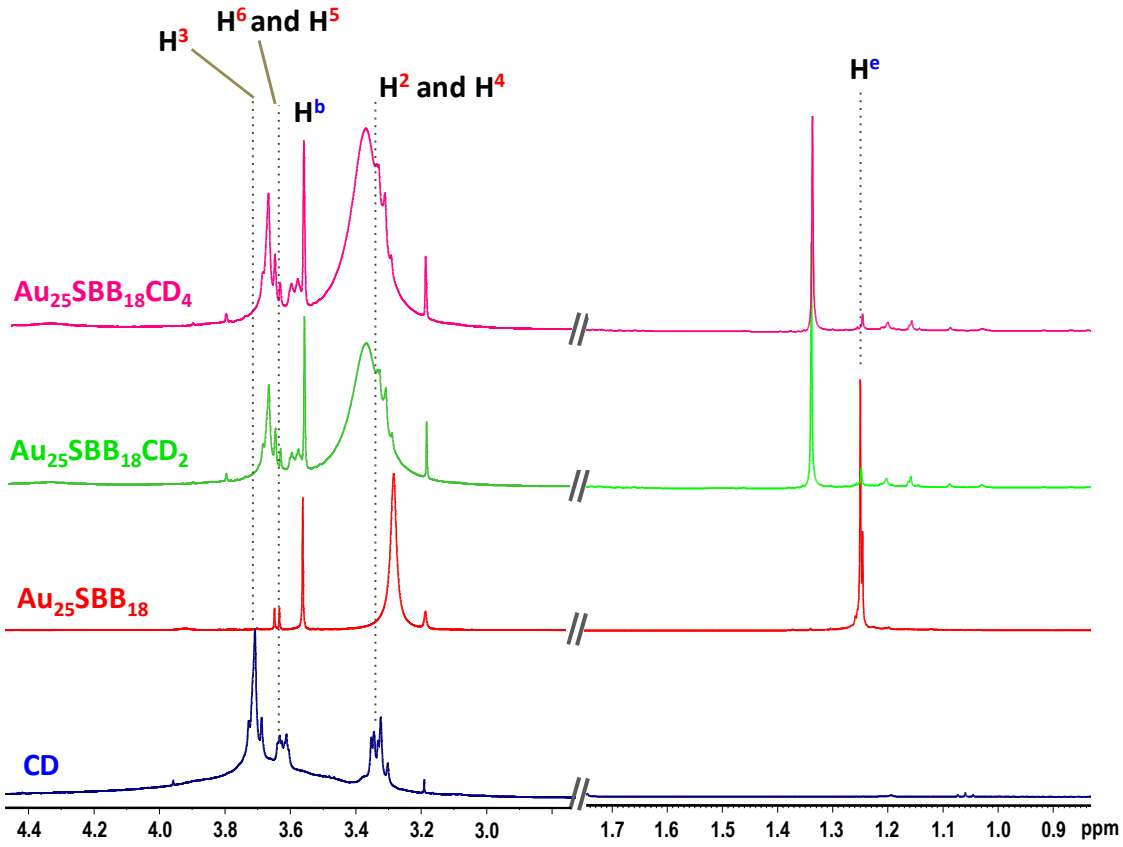

Figure S14. ^{1}H NMR of β-CD, $Au_{25}SBB_{18}$ and $Au_{25}SBB_{18}\cap CD_x$ in 1:1 solvent mixture of DMSO-d6 and $CDCl_3$ at 25 ^{o}C. Here signals due to unreacted H^e protons of BBS can also be observed (green and pink trace) which suggests the existence of free and complexed BBS on the cluster.

Supporting information 15

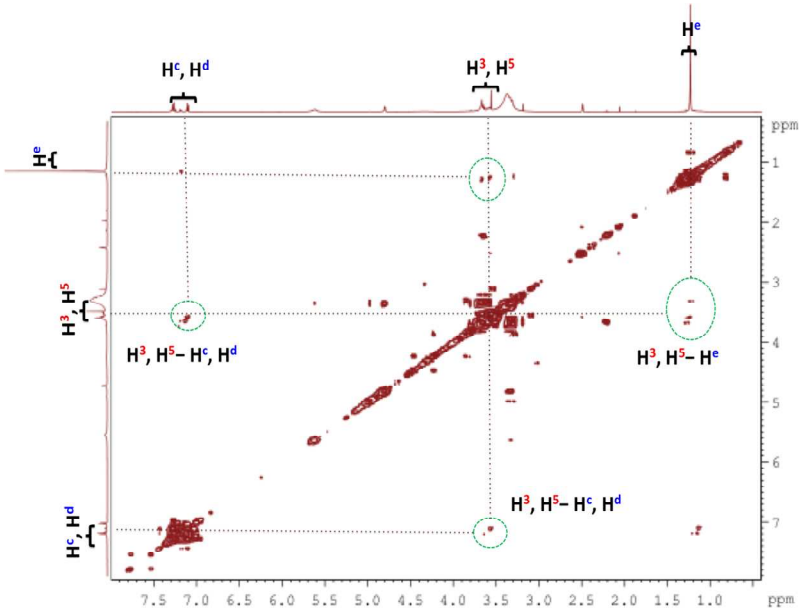

Figure 15. 2D COSY spectrum of $Au_{25}SBB_{18}\cap CD_4$ in 1:1 mixture of DMSO-d6 and $CDCl_3$ at 25 ^{o}C.

Supporting information 16

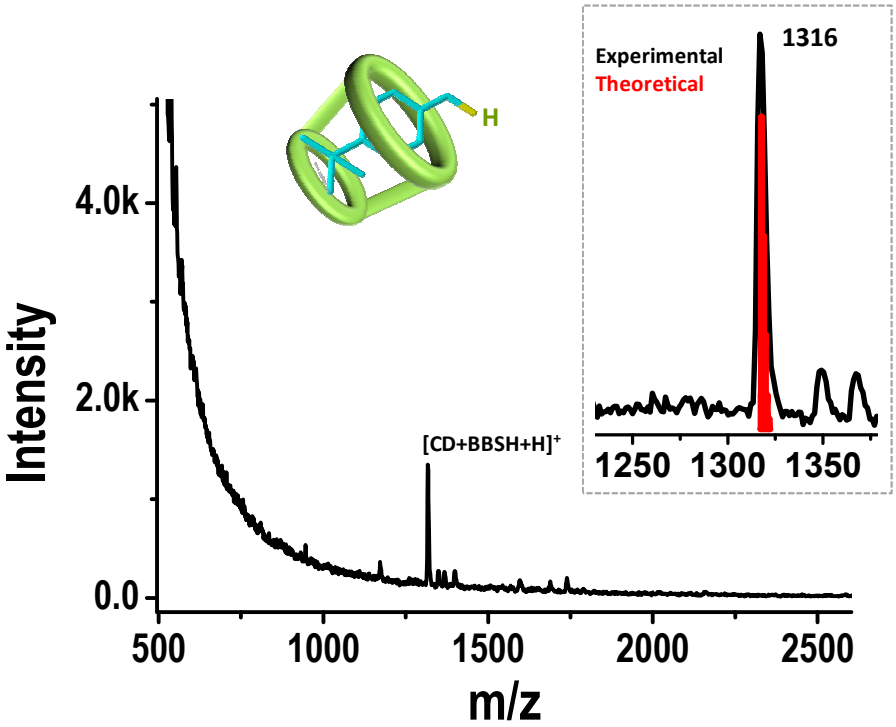

Figure S16. LDI MS of BBSH∩CD in the positive ion mode.

Supporting information 17

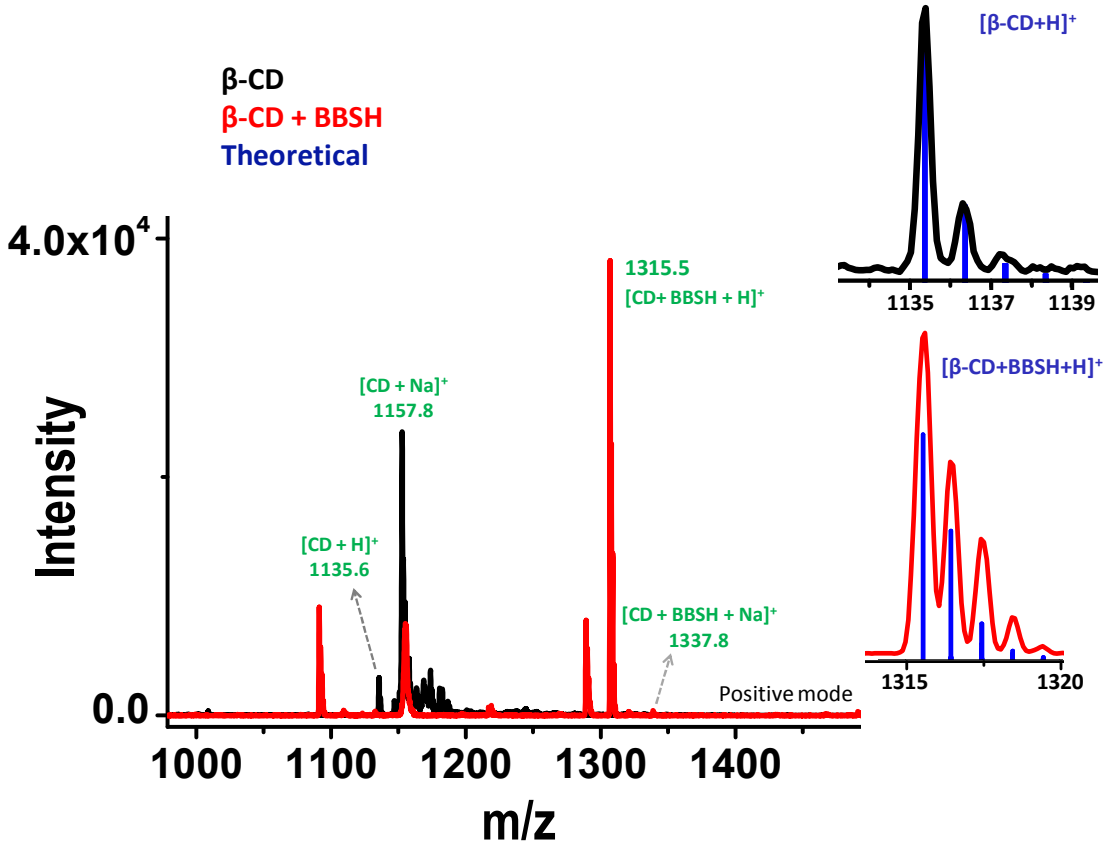

Figure S17a. ESI MS of β-CD and BBSH∩CD inclusion complex in the positive ion mode. Expanded views are given in the inset.

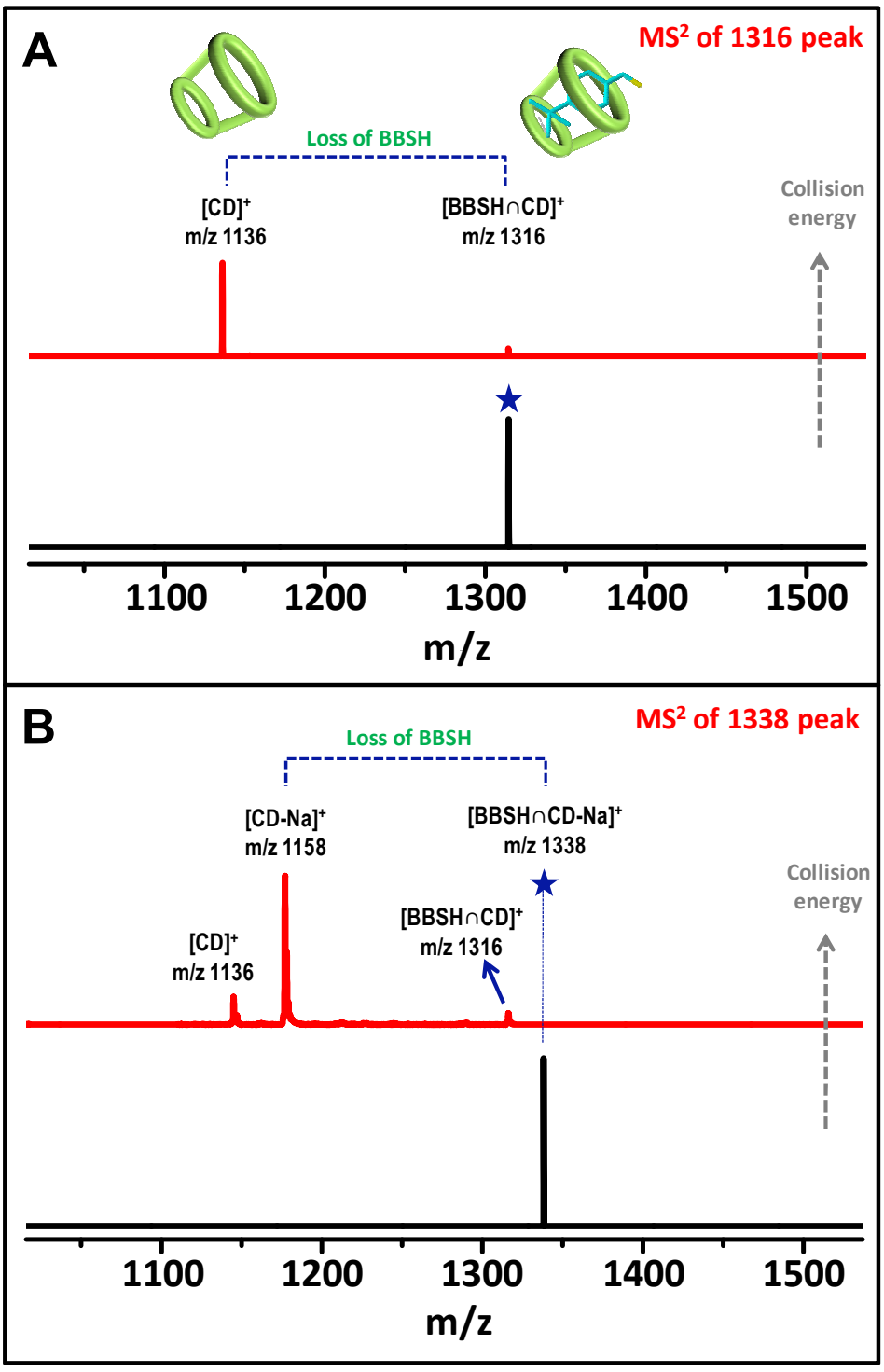

Figure S17b. Tandem mass ESI spectra (positive ion mode) for the peak at m/z 1316 (A) and 1338 (B) with increasing collision energy. Fragment ions are also marked. In the MS^2 spectrum of m/z 1338, the peaks formed at m/z 1158, 1316 and 1136 correspond to the loss of BBSH (180 Da) and Na (23 Da) from the parent ions.

Supporting information 18

The binding constant of a simple host-guest adduct, BBSH∩CD was measured in the same medium used for complexation of clusters using fluorescence spectral titrations.[6, 7] From the modified Benesi-Hildebrand equation, the linear plot of the reciprocal of the change in fluorescence intensity (ΔF) and the reciprocal of the molar concentration of cyclodextrin ($[CD]_0$) indicated a 1:1 stoichiometric complex with a binding constant of ~1776 M^{-1}. However, for $Au_{25}SBB_{18}$ and CD, such measurements using normal complexation titration, NMR, etc. were not attempted as multiple stoichiometries, $Au_{25}SBB_{18}∩CD_n$ (where n=1 to 4), can exist in solution thereby making calculation of binding constants difficult.

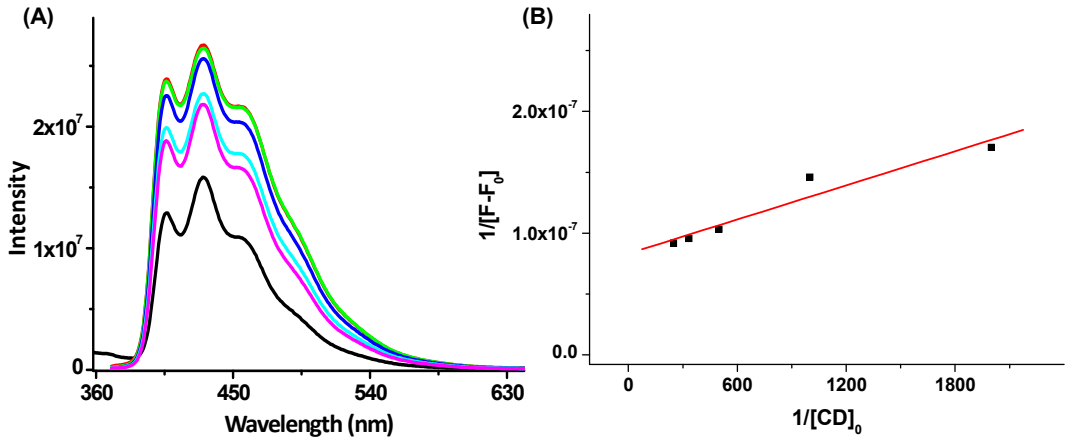

Figure S18. (A) Emission spectra of BBSH solution ($6.9*10^{-5}$ M) in THF/water mixture in the presence and absence of β-CD. From bottom to top: [β-CD] = 0, 0.5×10^{-3}, 1×10^{-3}, 2×10^{-3}, 3×10^{-3} and 4×10^{-3} M. (B) Plot of reciprocal of the change in fluorescence intensity (ΔF) and the reciprocal of the molar concentration of cyclodextrin ($[CD]_0$)

Supporting information 19

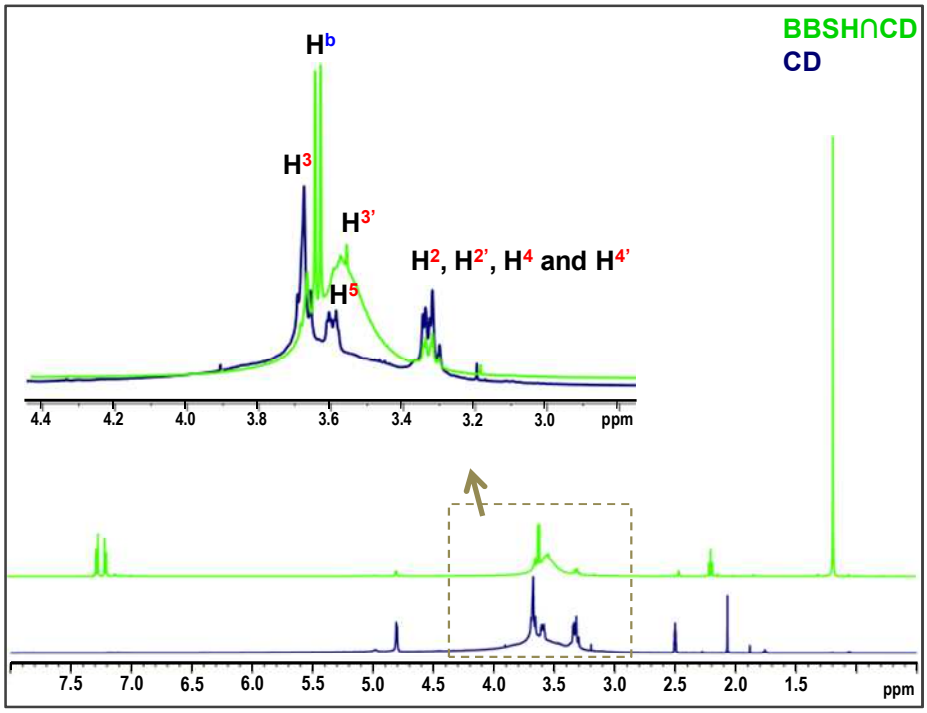

Figure 19a. Comparison of ^{1}H NMR of CD (blue trace) and BBSH∩CD (green trace) inclusion complex in 1:1 mixture of DMSO-d6 and $CDCl_3$ at 25 ^{o}C.

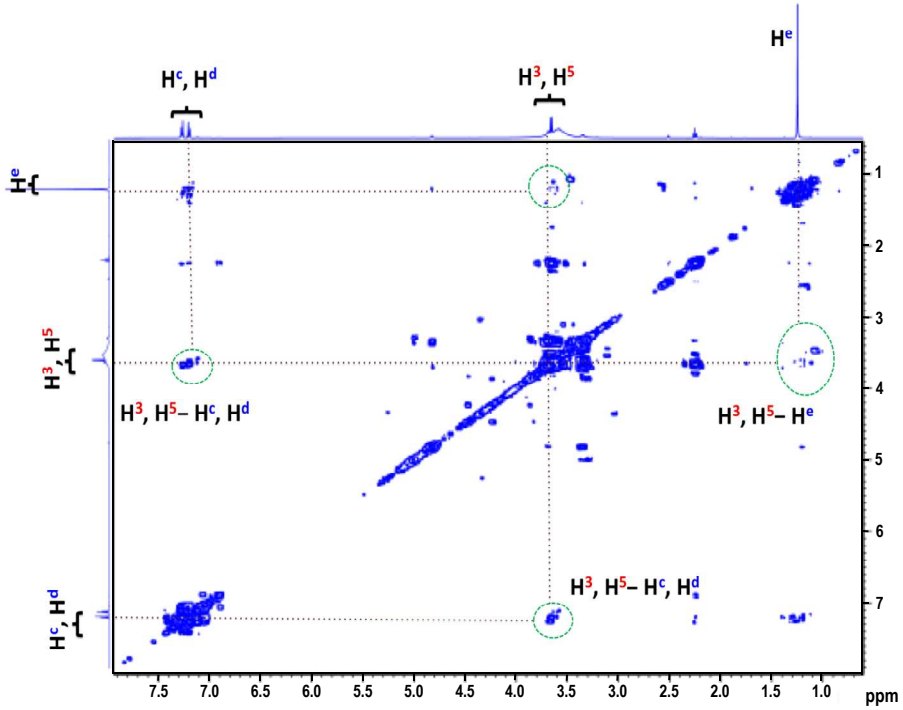

Figure 19b. 2D COSY spectrum of BBSH∩CD in 1:1 mixture of DMSO-d6 and $CDCl_3$ at 25 ^{o}C.

Supporting information 20

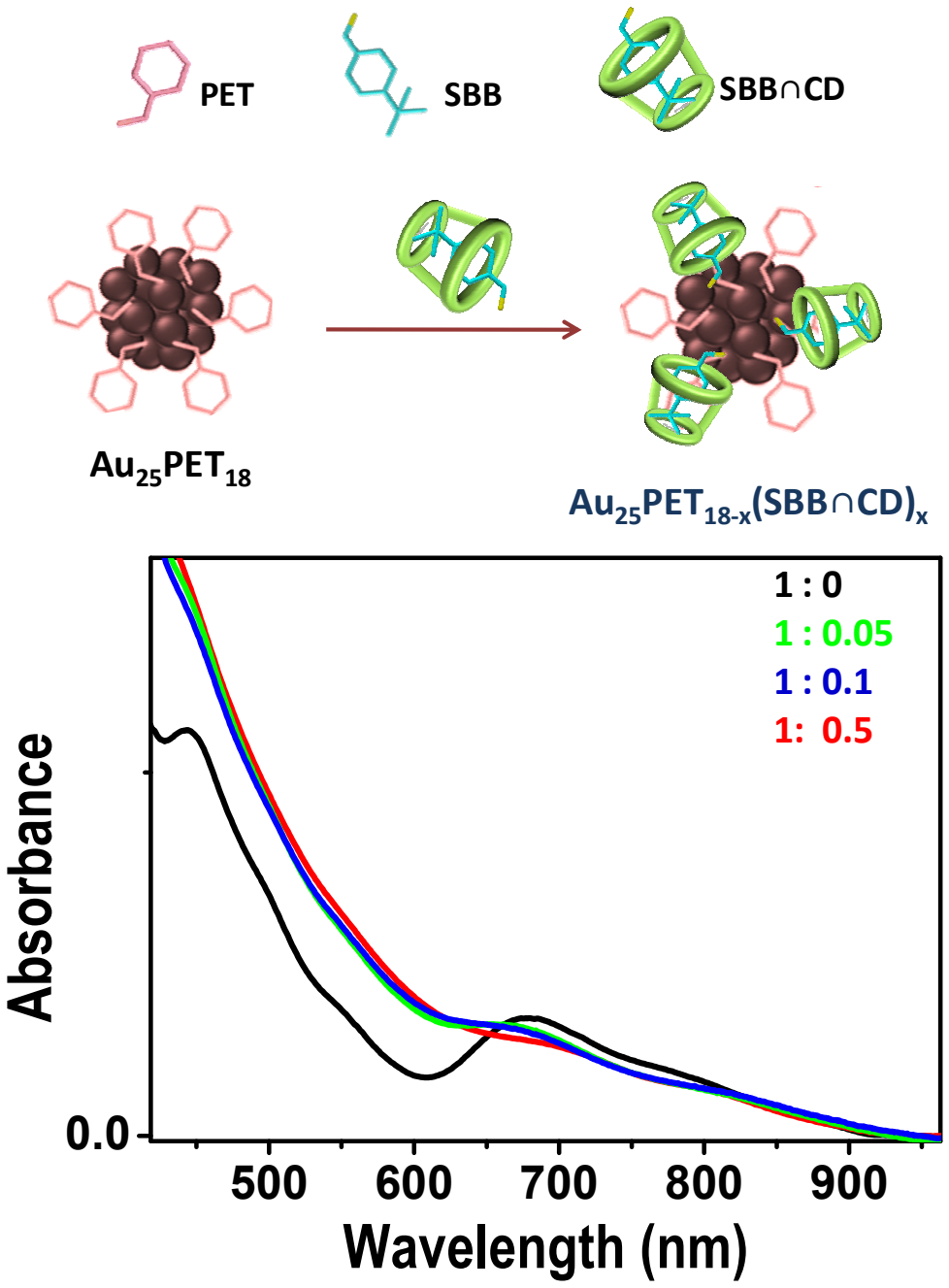

Figure S20. Effect of UV-vis absorption spectra after ligand exchange reaction of $Au_{25}PET_{18}$ with SBB∩CD (as incoming ligand). The PET:SBB∩CD ratios are shown.

Supporting information 21

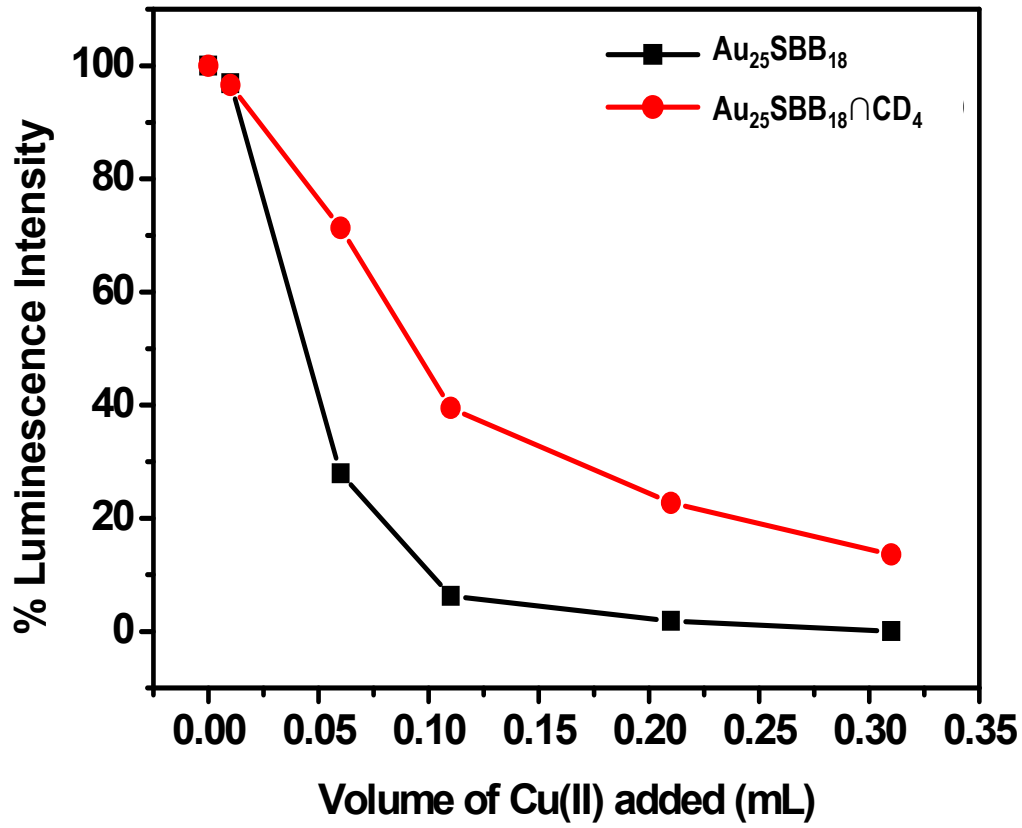

Figure S21. Quenching of (A) bare $Au_{25}SBB_{18}$ and (B) $Au_{25}SBB_{18}\cap CD_4$ upon treatment with an aqueous solution of 250 mM Cu^{2+} solution (note that clusters were taken in THF solvent so as to allow better miscibility). The spectra were measured after 5 minutes of addition.

Supporting information 22

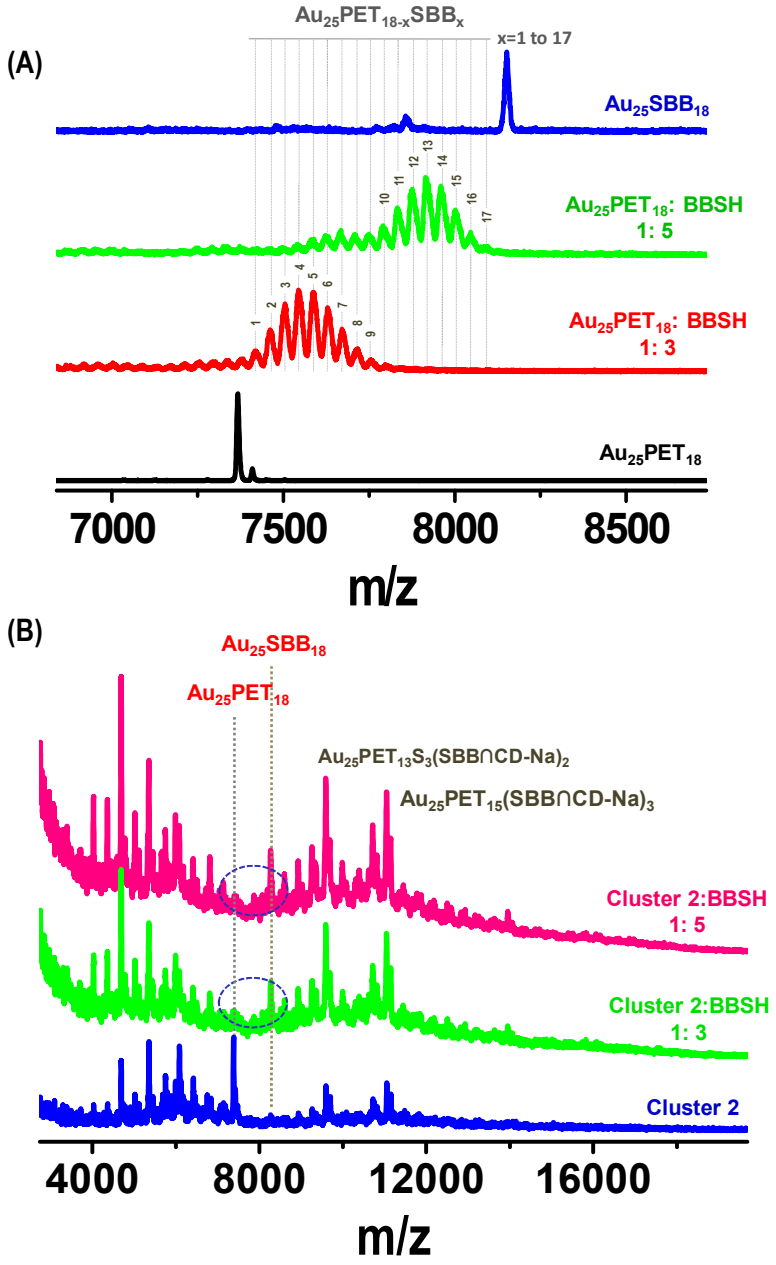

Figure S22. MALDI (L) mass spectra of bare $Au_{25}PET_{18}$ (A) and BBSH∩CD incorporated $Au_{25}PET_{18}$ QCs (denoted as 'Cluster 2' in the figure) (B) with excess BBSH thiol. In the case of $Au_{25}PET_{18}$ with excess BBSH (A), peaks corresponding to various ligand exchanged species, $Au_{25}PET_{18-x}SBB_x$ (where x=0 to 17) separated by m/z 42 due to the exchange of PET (MW 137.2) for BBS (MW 179.3), are seen under various conditions (labelled in figure). Spectrum corresponding to bare $Au_{25}SBB_{18}$ is also shown for comparison (blue trace in A). For (B), various amounts of BBSH was added to 'Cluster 2' which is a mixture of $Au_{25}PET_{18}$ and BBSH∩CD incorporated $Au_{25}PET_{18}$ QCs. While $Au_{25}PET_{18}$ ligand exchanges completely with BBSH to give a peak at m/z 8152 corresponding to $Au_{25}SBB_{18}$ (marked on the graph), peaks due to $Au_{25}PET_{15}(SBB∩CD\text{-}Na)_3$ and $Au_{25}PET_{13}S_3(SBB∩CD\text{-}Na)_2$ do not show any shift and their relative intensities are unaffected indicating the absence of ligand exchange.

Supporting information 23

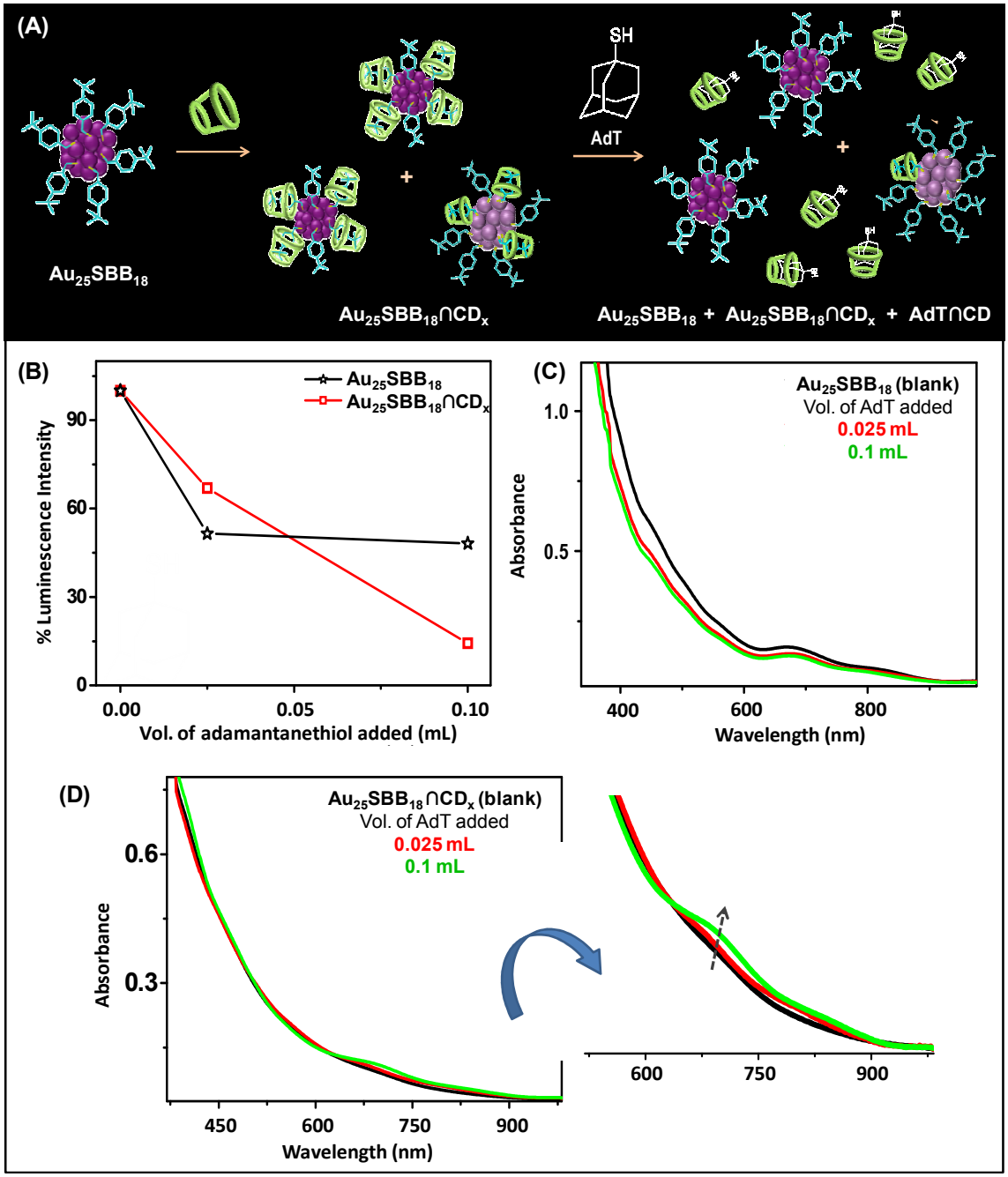

Figure S23. Effect of 1-adamantanethiol (AdT) on both $Au_{25}SBB_{18}$ and $Au_{25}SBB_{18}\cap CD_x$ was studied. Schematic of the possible events upon addition of AdT are depicted in (A). Luminescence from the QCs upon AdT addition is compared in (B). UV-vis absorption spectra of $Au_{25}SBB_{18}$ (C) and $Au_{25}SBB_{18}\cap CD_x$ (D), with addition of AdT are also shown. Re-appearence of Au_{25} absorption features with 0.1 mL of AdT (green trace, marked with an arrow) in $Au_{25}SBB_{18}\cap CD$ is observed in the expanded region of (D).

References:

1. Gaussian 09, Revision A.1. Frisch, M. J.; Trucks, G. W.; Schlegel, H. B.; Scuseria, G. E.; Robb, M. A.; Cheeseman, J. R.; Scalmani, G.; Barone, V.; Mennucci, B.; Petersson, G. *et al.* Gaussian, Inc., Wallingford CT, 2009.
2. Kleywegt, G. J., Crystallographic Refinement of Ligand Complexes. *Acta crystallographica. Section D, Biological crystallography* **2007,** *63*, 94-100.
3. http://www.chemspider.com/Chemical-Structure.2038012.html.
4. Snor, W. L. E., Weiss-Greiler P., Karpfen, A. , Viernstein, H., Wolschann, P., On the Structure of Anhydrous β-Cyclodextrin. *Chem. Phys. Lett.* **2007,** *441*, 159-162.
5. Boys, S. F.; Bernardi, F., The Calculation of Small Molecular Interactions by the Differences of Separate Total Energies. Some Procedures with Reduced Errors. *Molecular Physics* **1970,** *19*, 553-556.
6. Munoz de la Pena, A.; Ndou, T.; Zung, J. B.; Warner, I. M., Stoichiometry and Formation Constants of Pyrene Inclusion Complexes with β- and γ-Cyclodextrin. *The Journal of Physical Chemistry* **1991,** *95*, 3330-3334.
7. Wagner, B., The Use of Coumarins as Environmentally-Sensitive Fluorescent Probes of Heterogeneous Inclusion Systems. *Molecules* **2009,** *14*, 210-237